McCoy, S. J., Kamenos, N. A. , Chung, P., Wootton, T. J. and Pfister, C. A. (2018) A mineralogical record of ocean change: decadal and centennial patterns in the California mussel. *Global Change Biology*, 24(6), pp. 2554-2562.

There may be differences between this version and the published version. You are advised to consult the publisher's version if you wish to cite from it.

McCoy, S. J., Kamenos, N. A. , Chung, P., Wootton, T. J. and Pfister, C. A. (2018) A mineralogical record of ocean change: decadal and centennial patterns in the California mussel. *Global Change Biology*, 24(6), pp. 2554-2562. (doi:10.1111/gcb.14013)

http://eprints.gla.ac.uk/153200/

Deposited on: 07 December 2017

1   A mineralogical record of ocean change: decadal and centennial patterns in the California mussel

2

3   Running head:

4   A mineralogical record of ocean change

5

6   Sophie J. McCoy[1][*], Nicholas A. Kamenos[2], Peter Chung[2], J. Timothy Wootton[3], and Catherine

7   A. Pfister[3]

8

9   [1] Department of Biological Science, Florida State University, Tallahassee, FL 32306-4295

10   [2] School of Geographical and Earth Science, University of Glasgow, Glasgow, G12 8QQ,

11   Scotland

12   [3] Department of Ecology and Evolution, University of Chicago, Chicago, IL, 60637

13   [*] Corresponding author, mccoy@bio.fsu.edu

14

17

18   Paper type: Primary Research Article

19

20   **Abstract**

21   Ocean acidification, a product of increasing atmospheric carbon dioxide, may already have

22   affected calcified organisms in the coastal zone, such as bivalves and other shellfish.

23   Understanding species' responses to climate change requires the context of long-term dynamics.

24   This can be particularly difficult given the longevity of many important species in contrast to the

25   relatively rapid onset of environmental changes. Here, we present a unique archival dataset of

26   mussel shells from a locale with recent environmental monitoring and historical climate

27   reconstructions. We compare shell structure and composition in modern mussels, mussels from

28   the 1970s, and mussel shells dating back to 1000 to 2420 years BP. Shell mineralogy has

29   changed dramatically over the past 15 years, despite evidence for consistent mineral structure in

30   the California mussel, *Mytilus californianus*, over the prior 2,500 years. We present evidence for

31   increased disorder in the calcium carbonate shells of mussels and greater variability between

32   individuals. These changes in the last decade contrast markedly from a background of consistent

33   shell mineralogy for centuries. Our results use an archival record of natural specimens to

34   provide centennial-scale context for altered minerology and variability in shell features as a

35   response to acidification stress and illustrate the utility of long-term studies and archival records

36   in global change ecology. Increased variability between individuals is an emerging pattern in

37   climate change responses, which may equally expose the vulnerability of organisms and the

38   potential of populations for resilience.

39

40   **Introduction**

41   Current uncertainty regarding organismal responses to ongoing climate changes deals with the

42   juxtaposed issues of scale and mechanism: laboratory studies enable the isolation of a specific

43   stressor, while field studies are necessary to truly understand effects of a stressor in a natural,

44   often more variable, system. While field studies also can detect long-term evolutionary or

45   population dynamics (Hofmann *et al.*, 2010; Pfister *et al.*, 2016), the length of time required to

46   see a response can be prohibitive. Organisms that retain growth history records over millennial

47   timescales and that are relevant to contemporary environmental stressors offer a model to

48   overcome the challenge of long-term ecological relevance (Cobb *et al.*, 2003; Mann *et al.*, 2008;

49   Halfar *et al.*, 2013).

50

51   Calcified organisms such as bivalves are predicted to face the greatest challenges under future

52   ocean acidification (Cooley & Doney, 2009). Some coastal areas have already experienced large

53   changes in mean seawater acidity, in some cases equal to or greater than conditions originally

54   predicted in future ocean scenarios (Wootton *et al.*, 2008; Hofmann *et al.*, 2011; Wootton &

55   Pfister, 2012; Wahl *et al.*, 2015; Kroeker *et al.*, 2016; Chan *et al.*, 2017). For example, seawater

56   pH has declined rapidly in the northeast Pacific over the last 17 years, accompanied by changes

57   in δ^{13}C signatures from mussel shells, which reveal altered inorganic carbon chemistry over

58   recent decades (Pfister *et al.*, 2011).

59

60   Calcification can be affected by multiple environmental parameters, including pCO_2 (Kroeker *et*

61   *al.*, 2010; Gazeau *et al.*, 2013; Fitzer *et al.*, 2014; Pfister *et al.*, 2016), temperature (Fitzer *et al.*,

62   2015), wave exposure (Fox & Coe, 1943), food availability (Coe, 1945; Thomsen & Melzner,

63   2010; Hahn *et al.*, 2011; Waldbusser *et al.*, 2013), predation pressure (Vermeij, 1976), and their

64   interacting effects (Melzner *et al.*, 2011; Kroeker *et al.*, 2017). These calcification responses

65   include changes in growth rate and overall size (Thomsen & Melzner, 2010), changes in shell

66   morphology (Fitzer *et al.*, 2015; Pfister *et al.*, 2016), and mineralogical plasticity (Nash *et al.*,

67   2012; Pauly *et al.*, 2015). Mineralogical plasticity has been proposed as a potentially beneficial

68   adaptive mechanism (Fitzer *et al.*, 2014; Leung *et al.*, 2017) that allows calcified organisms to

69   continue growth under acidified conditions. However, ecological and physiological trade-offs

70   exist between mineralogy, morphology, and mineral strength that can lead to ecological

71   repercussions of environmentally induced skeletal changes (McCoy & Pfister, 2014; McCoy &

72   Ragazzola, 2014), and changes in mussel shell shape or thickness may be detrimental to their

73   survival in natural conditions (Gooding *et al.*, 2009; Fitzer *et al.*, 2015; Pfister *et al.*, 2016).

74   Laboratory studies have shown mineralogical changes to occur over relatively short timescales

75   (< 6 months) in both adults and juveniles (Melzner *et al.*, 2011; Fitzer *et al.*, 2014; 2016) and to

76   be especially important to larval and other early developmental stages (Stumpp *et al.*, 2011;

77   Waldbusser *et al.*, 2013; Thomsen *et al.*, 2015).

78

79   While specific calcification mechanisms in bivalves remain definitively unknown (Thomsen *et*

80   *al.*, 2015), amorphous calcium carbonate, which lacks clear crystallographic structure, has been

81   suggested as a precursor to calcium carbonate crystals. Amorphous calcium carbonate is

82   produced within an intracellular compartment and transported to the site of calcification (Mount

83   *et al.*, 2004; Weiner & Addadi, 2011), where it can either remain amorphous or crystallize into

84   aragonite or calcite as dictated by the presence of matrix proteins (Weiss *et al.*, 2002; Jacob *et*

85   *al.*, 2008). The production of costly matrix proteins necessary to complete the calcification

86   process may be reduced under stress, resulting in longer persistence of amorphous calcium

87   carbonate (Palmer, 1983; Fitzer *et al.*, 2016).

88

89   Whether an organism produces aragonite or calcite may also reflect local conditions. Aragonite

90   is more soluble than the calcite polymorph of calcium carbonate, and therefore at greater risk of

91   dissolution from elevated pCO_2 (Feely *et al.*, 2012). Under ocean-wide ocean-acidification

92   conditions predicted to occur by 2001, saturation of aragonite in the surface ocean will decline

93   faster than that of calcite and cause dissolution of aragonitic shells, such as those of planktonic

94   pteropods (Orr *et al.*, 2005) and benthic corals and mollusks (Hall-Spencer *et al.*, 2008).

95   Seawater magnesium concentrations may also mediate how calcium carbonate structures are

96   made (Ries, 2005). Thermodynamically, aragonite or high-Mg calcite precipitation is favored

97   when seawater concentrations of Mg are elevated, and calcite precipitation is favored when

98   seawater Mg concentrations are low (Ries *et al.*, 2008). A similar mechanism was documented

99   in typically high-Mg calcite coralline algae, which were more resistant to ocean acidification

100   when their skeletons included the stable Mg-bearing carbonate dolomite (Nash *et al.*, 2012).

101   Thus, crystal phase, crystal structure, and carbonate Mg content are all potential causes of

102   mineralogical variation in response to ocean acidification. Possible responses include those that

103   may be beneficial to organisms in the long-term, such as mineralogical shifts to more stable

104   carbonate polymorphs. However, other responses may be driven by short-term energetic effects

105   that will result in weaker or more soluble shells, perhaps conversely to short-term ecological

106   forces, such as predation.

107

108   The California mussel, *Mytilus californianus*, ranges from Alaska to Baja California along the

109   coastline of the eastern Pacific Ocean, which experiences seasonal upwelling of acid seawater

110   (Feely *et al.*, 2008). *M. californianus* lays down an additional region of inner prismatic calcite, a

111   shell layer which is unique to *M. californianus* among mussel species worldwide (Dodd, 1964).

112   This trait may have evolved in response to long-term local acidification via upwelling in the

113   California Current System to protect the aragonitic nacreous layer, and it is present in our

114   midden shell samples dating back to AD 663. Regardless of its origin, it will likely be

115   advantageous to *M. californianus* as ocean pH declines and its surroundings become more

116   corrosive.

117

118   Previous work has shown that the thickness of annual growth bands within the inner prismatic

119   layer of *M. californianus* is reduced by approximately half when comparing modern day

120   specimens to shells dated to 1000-1340 years BP at Tatoosh Island, WA (Pfister *et al.*, 2016),

121   suggesting that modern shells may be experiencing stress associated with biomineralization

122   through time. Here, we present a study of shell structure from the California mussel, *M.*

123   *californianus*, spanning decadal and centennial scales to determine the long-term effects of

124   changes in ocean carbon chemistry on shell mineralogy in a natural system. Alterations to

125   modern shells that would be expected if calcification is increasingly stressful or costly may

126   include: a changed crystal structure, increases in the less soluble calcite polymorph, and

127   increased Mg content in the $CaCO_3$ lattice. Reduced mineral organization was interpreted as a

128   possible effect of increased energy load of biomineralization, while increased variability between

129   shells within a time period suggests environmental stress.

130

131   **Materials and Methods**

132   ***Sample collection and preparation***

133   *Mytilus californianus* were collected live from Tatoosh Island, WA (48.32° N, 127.74° W) in

134   spring of 2009, 2011, and 2015 at two sites, N- and SW-facing, on the island. Adult *M.*

135   *californianus* from two locations at Sand Point (48.126° N, 124.702° W), Sand Point North and

136   Yellow Banks, were collected in July and August 2010. These collections comprise the

137   'modern' sampling effort. 'Archival' shells were collected live from Tatoosh Island in the 1970s

138   by T. Suchanek from a SW-facing region of the island. Excavation of Native American middens

139   from the Makah Tribe (McMillan, 2000), who used Tatoosh Island as a summer camp prior to

140   the 1800s and historically had a large settlement at Sand Point, provided 'midden' valves from

141   Tatoosh Island through the Makah Cultural and Resource Center, while Sand Point midden

142   material was provided by the Olympic National Park. These shells were radiocarbon dated using

143   shell material from their most recent year of growth, with Tatoosh Island midden shells dated to

144   1000-1340 years BP in 2010 (Pfister *et al.*, 2011) and Sand Point midden shells dated to 2150-

145   2440 years BP in 2015 (Pfister *et al.*, 2016). Valves were cross-sectioned along their axis of

146   maximum growth using a slow-speed saw with a diamond blade to make a 3mm-thick cross

147   section. Cross-sections were mounted on glass slides and polished on 800-4000 grit silicon

148   carbide paper, followed by aluminum oxide (0.3 and 1 μm) and colloidal silica (0.6 μm)

149   suspensions. Cross-sections were scanned at high resolution prior to analysis to provide a

150   sample image map.

151

152   ***EBSD imaging***

153   Electron backscatter diffraction (EBSD) was performed to image the crystallographic orientation

154   of shell calcite. A 20 kV beam voltage was utilized under low vacuum mode (~50 Pa) on an FEI

155   Quanta 200 F Environmental SEM (University of Glasgow, School of Geographical and Earth

156   Science), with a stage tilt of 70° to detect backscatter Kikuchi patterns (Pérez-Huerta *et al.*,

157   2009). Scans were conducted within the inner prismatic layer of *M. californianus*, well outside

158   of the beak area (Dodd, 1964) Fig. S1. In shells HC09006 (modern, collected live in 2009) and

159   TI09001 (midden, radiocarbon aged to 1170 yBP), full transects were imaged from the outermost

160   (oldest shell growth) to the innermost (youngest) calcite bands at 0.5 μm resolution. In shells

161   HC15003, HC15004, GL15005, GL15007 (modern, 2015), GL09002 (modern, 2009), TS10002,

162   TS10004 (archival, 1975), TI09001 (midden, 1170 yBP), TI09004 (midden, 1100 yBP), TI09007

163   (midden, 1060 yBP) and TI09008 (midden, y1050 BP), a section containing one full summer and

164   winter growth cycle from the middle of the shell (to avoid possible age effects from young or

165   elderly growth layers) was imaged at 1.1 μm resolution. Crystallographic orientation maps were

166   produced using OIM Analysis software v. 7.

167

168   ***Raman spectroscopy***

169   Transects were taken from the outermost (oldest) to innermost (youngest) calcite bands in all

170   shells from Tatoosh Island (modern, n=15; archival, n=5, midden, n=7) and Sand Point (modern,

171   n=10; midden, n=8). Points were chosen manually at 20x magnification. Replication of 3-4x

172   within a growth band was taken at random across samples to test within-sample variability.

173   Raman spectra were taken using the 785 nm near-infrared laser. Acquisition time was set to 1.00

174   s at 100% laser power for 10x accumulations per sample point (Pauly *et al.*, 2015). Peaks were

175   identified manually and fit using Wire software v. 4.2. Analyses were conducted on all samples

176   from all shells pooled. Mg-O bond strength was determined from the full width at half peak

177   maximum (FWHM) of the Raman shift peak centered at ~1089 cm^{-1} and relative Mg

178   concentrations were determined from the exact position of the peak (Bischoff *et al.*, 1985; Pauly

179   *et al.*, 2015).

180

181   **Results**

182   *Crystallographic orientation*

183   Electron backscatter diffraction (EBSD) provides a qualitative measure of crystallographic

184   orientation. Comparison of *M. californianus* shell growth from 1050-1170 AD (midden), the

185   1970s (archival), 2000s (modern) and 2010s (modern) revealed visually-apparent changes in

186   crystal orientation and crystal size among shell material deposited in the 2010s compared with all

187   other time intervals (Fig. 1-4). Shells from 1050-1170 AD show visual signs of fragility and

188   light wear, likely from the degradation of the organic matrix that sheaths the calcium carbonate

189   crystals during their ~1,000 years spent in middens. However, these midden shells provide a

190   clear record of calcite crystal organization and uniformity of crystal orientation, as does shell

191   material deposited in the 1970s and 2000s (Fig. 1-3). Shell material from the 2010s (collected in

192   2015) documents mosaic patterns of crystal orientation, greater disorder among crystals, smaller

193   crystal sizes, and possible regions of disorganized or recrystallized calcium carbonate (Fig. 4).

194   We also observed greater variation in crystal orientation and size between shells in these most

195   recent samples (Fig. 4).

196

197   *Shell Composition and Bond Strength*

198   The low frequency vibrations detected by Raman spectroscopy indicate the elemental

199   composition and types of bonds present in solid materials. Mg is present as a trace element in all

200   natural marine carbonates. The Raman vibrational peak at ~1089 cm^{-1} has been identified as an

201   Mg-O bond and its location is one of the peaks used to differentiate calcite and aragonite

202   (Bischoff *et al.*, 1985). Full width at half peak maximum (FWHM) is related to the strength of

203   the Mg-O bond, while Raman shift of the ~1089 cm^{-1} peak is a proxy of Mg content of calcite

204   (Pauly *et al.*, 2015).

205

206   Pooled between sites, Tatoosh Island, WA and nearby Sand Point, WA on the mainland, there

207   was a poor relationship between increases in FWHM and Raman shift on a per sample basis

208   (a=0.858, r^2 = 0.238, p=0.405; Fig. 5a). Mean FWHM increased over time from midden to

209   modern samples from 4.3 to 4.6 (7%) at Tatoosh Island, and from 4.5 to 4.6 at Sand Point (2%)

210   (t-test on shell means; TI: t_{15}=5.46, p<0.001, SP: t_9=1.38, p=0.198), marking a temporal decline

211   in Mg-O bond strength (Fig. 5a). Mean Raman shift increased at Tatoosh from 1086.75 to

212   1086.89 cm^{-1}, indicating increasing Mg concentration, but declined at Sand Point from 1086.85

213   to 1086.72 cm^{-1}, indicating a decline in Mg concentration (t-test on shell means; TI: t_{16}=5.67,

214   p<0.001, SP: t_9=-3.02, p=0.014; Fig. 5a). Archival (1970s) and modern (1990s, 2000s, 2010s)

215   samples did not differ in FWHM (t-test on shell means; archival mean 4.55, modern mean 4.61

216   cm^{-1}; TI: t_{16}=0.899, p=0.383) or in Raman shift (t-test on shell means; archival mean 1086.87,

217   modern mean 1086.89 cm^{-1}; TI: t_{17}=0.850, p=0.407). Raman shift increased with ontogeny

218   within each shell at both sites (linear mixed-effects model with individual shell as a random

219   effect, individual age as a fixed effect; TI: coeff.=0.0064, p<0.001, number of meas.=615,

220   number of shells =27; SP: coeff.=0.0156, p<0.001, number of meas.=174, number of shells =18;

221   Fig. S8, S9) but FWHM showed no significant ontogenetic trend (linear mixed-effects model

222   with individual shell as a random effect, individual age as a fixed effect; TI: coeff.=0.0019,

223   p=0.426, number of meas.=615, number of shells =27; SP: coeff.=0.0055, p=0.251, number of

224   meas.=174, number of shells =18; Fig. S8, S9).

225

226   *Increased variability in shell structure over time*

227   Overall, variance in both bond strength and Mg content between individuals increased in modern

228   samples. Standard deviation (SD) in FWHM increased from 0.19 to 0.35 (34%) at Sand Point

229   ($F_{6,14}$=32.3, p=0.004) but did not show a significant change at Tatoosh Island, despite a 25%

230   increase from 0.24 to 0.30 ($F_{6,14}$=2.82, p=0.210). SD in Raman shift increased from 0.112 to

231   0.162 (144%) at Tatoosh Island ($F_{6,14}$=32.3, p=0.004) and from 0.058 to 0.281 (484%) at Sand

232   Point ($F_{7,9}$=38.4, p<0.001) between midden and modern shells (Fig. 5b). The increased

233   variability in *M. californianus* Mg-O bond strength is not fully explained by the variability in Mg

234   content (Fig. 5b; linear model r^2 = 0.72, p=0.068).

235

236   **Discussion**

237   Measures of qualitative and quantitative shell traits over multiple adult individuals at two nearby

238   sites allow for the robust detection of trends over time in a natural system and for measurement

239   of inter-individual variability in those traits. Increased trait variability corresponds to an

240   expectation of greater phenotypic plasticity under increased environmental stress. Trait values,

241   including shell mineralogy, lead to fitness trade-offs (i.e. metabolic energy used to biomineralize,

242   shell thickness to withstand predation or disturbance, growth rates), which may lead to selection

243   for plastic developmental traits in unpredictable environments (Stearns, 1989). Similarly,

244   stressful environments can select for genotypes that produce adaptive, reversible, plastic

245   phenotypes (Gabriel, 2005).

246

247   Mg-O bond strength variability typically indicates increased positional disorder, or rotation of

248   the CO_3^{2-} molecule out of the basal plane (Bischoff *et al.*, 1985). This substantial increase in

11

249   variability in Mg-O and Mg content in modern samples is also reflected in the significant, yet

250   irregular, trends we observe in both metrics, and likely drives the inconsistency in directional

251   change over time. This interpretation is compatible with our EBSD data, which shows increased

252   variability in the orientation of $CaCO_3$ crystal units (changes in color, Fig. 1-4) and decreased

253   crystal size.

254

255   Our EBSD data for *M. californianus* are consistent with observations in *M. edulis* (Fitzer *et al.*,

256   2016), which also displayed reduced control over crystallographic orientation of calcite under

257   experimental ocean acidification of 1000 μatm pCO_2, similar to acidification conditions reported

258   in the present day at Tatoosh Island (Wootton & Pfister, 2012) and in other coastal systems

259   (Hofmann *et al.*, 2011; Wahl *et al.*, 2015). In *M. edulis,* increased crystallographic variability

260   has been attributed to an increase in amorphous calcium carbonate in both aragonitic and calcitic

261   crystal phases (Fitzer *et al.*, 2016). Raman data, however, suggest that *M. californianus*

262   predominantly continues to precipitate calcite crystals. EBSD scans show that those crystals

263   become increasingly disorganized and fine-grained in our most recent 2015 samples.

264

265   This decadal and centennial time series of shells enabled us to study population-scale responses

266   to 'natural' acidification over time. Yet, the rapid onset of the severity of recent pH excursions

267   suggested by $\delta^{13}C$ concentrations from these same shells (Pfister *et al.*, 2011) relative to the

268   length of our record suggests that adaptation or acclimatization in subsequent generations to

269   these most recent changes may still be forthcoming. Our study used only adult *M. californianus*,

270   a long-lived species relative to its congeners. It is noteworthy that *M. edulis* juveniles spawned

271   from parents living in experimental acidified conditions grew shells containing only calcite, in

272   contrast to the bimineralic (aragonitic and calcitic) shells of their parents (Fitzer *et al.*, 2014).

273

274   Other, aragonite-containing *Mytilus* species have shown a diversity of responses to changes in

275   seawater carbonate chemistry, including decreased size and shell thickness during larval stages,

276   decreases in shell density, shell dissolution, and weakened byssal threads (Thomsen *et al.*, 2010;

277   Gaylord *et al.*, 2011; O'Donnell *et al.*, 2013; Fitzer *et al.*, 2014; 2015; 2016). *M. californianus*

278   shell mineralogy should be more resistant to ocean acidification compared with other bivalves

279   because it is the only mussel to lay down calcite instead of aragonite in its inner shell layer

280   (Dodd, 1964), which is exposed to ambient seawater when mussels are feeding at high tide. This

281   trait may explain its ability to continue biomineralizing under reduced pH conditions.

282

283   Because *M. californianus* is almost exclusively found in the already-acidic California current

284   system, its inner prismatic calcite layer may represent a plastic or evolutionary response to long-

285   term acidification stress in this region, over hundreds or possibly thousands of years. EBSD

286   scans spanning all growth layers of midden shells indicate that *M. californianus* has grown a

287   calcitic inner prismatic layer for at least 1,000 years. However, the inner prismatic calcite layer

288   in *M. californianus* has thinned by half (Pfister *et al.*, 2016), despite changing seawater carbon

289   chemistry over the same interval (Pfister *et al.*, 2011). Thus, the number of deleterious effects of

290   ocean acidification demonstrated for *M. californianus* suggests that it is still vulnerable to ocean

291   acidification effects, including ad-hoc biomineralization as acidification continues. Together

292   with possible niche constriction as its upper elevational limit becomes restricted by increasing

293   temperatures (Harley, 2011), this forms an alarming prognosis for the future of *M. californianus*,

294 a foundational species that supports hundreds of associated organisms in its bed structure

295 (Suchanek, 1992).

296

297 Our results reveal increased disorder in the calcium carbonate shells of the California mussel, *M.*

298 *californianus*, as a result of increased acidification. Shell mineralogy has altered dramatically

299 over the past 15 years, despite evidence for 2,500 years of consistent mineral structure in the

300 calcitic inner prismatic layer. Increased shell structure variability, in particular, has emerged as a

301 primary response to acidification stress in shell formation in adult *M. californianus*, despite an

302 expectation of increased resistance to acidification based on the shell mineralogy of this *Mytilus*

303 species. Increased variability is a theme that has emerged over terrestrial and marine climate

304 change responses at the broadest scale (Inouye, 2008; Kroeker *et al.*, 2010; Ovaskainen &

305 Skorokhodova, 2013; CaraDonna *et al.*, 2014), reflecting differential fragilities and trade-offs

306 that may affect survival between genotypes, populations, or microhabitats. While increases in

307 variability reveal the vulnerability of organisms to environmental changes, they may also

308 indicate potential for resilience or recovery.

309

316

326

327   **References**

328   Bischoff WD, Sharma SK, MacKenzie FT (1985) Carbonate ion disorder in synthetic and
329   biogenic magnesian calcites: a Raman spectral study. *American Mineralogist*, **70**, 581−589.
330   CaraDonna PJ, Iler AM, Inouye DW (2014) Shifts in flowering phenology reshape a subalpine
331   plant community. *Proceedings of the National Academy of Sciences of the United States of*
332   *America*, **111**, 4916−4921.
333   Chan F, Barth JA, Blanchette CA et al. (2017) Persistent spatial structuring of coastal ocean
334   acidification in the California Current System. *Scientific Reports*, **7**, 255−7.
335   Cobb KM, Charles CD, Cheng H, Edwards RL (2003) El Niño/Southern Oscillation and tropical
336   Pacific climate during the last millennium. *Nature*, **424**, 271−276.
337   Coe WR (1945) Nutrition and growth of the California Bay-mussel (*Mytilus edulis diegensis*).
338   *Journal of Experimental Zoology*, **99**, 1−14.
339   Cooley SR, Doney SC (2009) Anticipating ocean acidification's economic consequences for
340   commercial fisheries. *Environmental Research Letters*, **4**, 024007.
341   Dodd JR (1964) Environmentally controlled variation in the shell structure of a pelecypod
342   species. *Journal of Paleontology*, **38**, 1065−1071.
343   Feely RA, Sabine CL, Byrne RH et al. (2012) Decadal changes in the aragonite and calcite
344   saturation state of the Pacific Ocean. *Global Biogeochemical Cycles*, **26**, GB3001.
345   Feely RA, Sabine CL, Hernandez-Ayon JM, Ianson D, Hales B (2008) Evidence for upwelling of
346   corrosive "acidified" water onto the continental shelf. *Sciencexpress*, 1−3.
347   Fitzer SC, Chung P, Maccherozzi F, Dhesi SS, Kamenos NA, Phoenix VR, Cusack M (2016)
348   Biomineral shell formation under ocean acidification: a shift from order to chaos. *Scientific*
349   *Reports*, **6**, 21076.
350   Fitzer SC, Cusack M, Phoenix VR, Kamenos NA (2014) Ocean acidification reduces the
351   crystallographic control in juvenile mussel shells. *Journal of Structural Biology*, 1−22.

352 Fitzer SC, Vittert L, Bowman A, Kamenos NA, Phoenix VR, Cusack M (2015) Ocean
353   acidification and temperature increase impact mussel shell shape and thickness: problematic
354   for protection? *Ecology and Evolution*, **5**, 4875–4884.
355 Fox DL, Coe WR (1943) Biology of the California sea-mussel (*Mytilus californianus*). II.
356   Nutrition, metabolism, growth and clacium deposition. *Journal of Experimental Biology*,
357   **205**, 205–249.
358 Gabriel W (2005) How stress selects for reversible phenotypic plasticity. *Journal of evolutionary*
359   *biology*, **18**, 873–883.
360 Gaylord B, Hill TM, Sanford E et al. (2011) Functional impacts of ocean acidification in an
361   ecologically critical foundation species. *Journal of Experimental Biology*, **214**, 2586–2594.
362 Gazeau F, Parker LM, Comeau S et al. (2013) Impacts of ocean acidification on marine shelled
363   molluscs. *Marine Biology*, **160**, 2207–2245.
364 Gooding RA, Harley CDG, Tang E (2009) Elevated water temperature and carbon dioxide
365   concentration increase the growth of a keystone echinoderm. *Proc. Natl. Acad. Sci.*, **106**,
366   9316–9321.
367 Hahn S, Rodolfo-Metalpa R, Griesshaber E et al. (2011) Marine bivalve geochemistry and shell
368   ultrastructure from modern low pH environments. *Biogeosciences Discuss.*, **8**, 10351–
369   10388.
370 Halfar J, Adey WH, Kronz A (2013) Arctic sea-ice decline archived by multicentury annual-
371   resolution record from crustose coralline algal proxy.
372 Hall-Spencer JM, Rodolfo-Metalpa R, Martin S et al. (2008) Volcanic carbon dioxide vents
373   show ecosystem effects of ocean acidification. *Nature*, **454**, 96–99.
374 Harley CDG (2011) Climate change, keystone predation, and biodiversity loss. *Science*, **334**,
375   1124–1127.
376 Hofmann GE, Barry JP, Edmunds PJ, Gates RD, Hutchins DA, Klinger T, Sewell MA (2010)
377   The Effect of Ocean Acidification on Calcifying Organisms in Marine Ecosystems: An
378   Organism-to-Ecosystem Perspective. *Annual Review of Ecology, Evolution, and Systematics*,
379   **41**, 127–147.
380 Hofmann GE, Smith JE, Johnson KS et al. (2011) High-Frequency Dynamics of Ocean pH: A
381   Multi-Ecosystem Comparison (ed Chin W-C). *PLoS ONE*, **6**, e28983–11.
382 Inouye DW (2008) Effects of climate change on phenology, frost damage, and floral abundance
383   of montane wildflowers. *Ecology,* **89**, 353-362.
384 Jacob DE, Soldati AL, Wirth R, Huth J, Wehrmeister U, Hofmeister W (2008) Nanostructure,
385   composition and mechanisms of bivalve shell growth. *Geochimica et Cosmochimica Acta*,
386   **72**, 5401–5415.
387 Kroeker KJ, Kordas RL, Harley CDG (2017) Embracing interactions in ocean acidification
388   research: confronting multiple stressor scenarios and context dependence. *Biology Letters*,
389   **13**, 20160802–4.
390 Kroeker KJ, Kordas RL, Crim RN, Singh GG (2010) Meta-analysis reveals negative yet variable
391   effects of ocean acidification on marine organisms. *Ecology Letters*, **13**, 1419–1434.
392 Kroeker KJ, Sanford E, Rose JM et al. (2016) Interacting environmental mosaics drive
393   geographic variation in mussel performance and predation vulnerability. *Ecology Letters*, **19**,
394   771–779.
395 Leung JYS, Russell BD, Connell SD (2017) Mineralogical Plasticity Acts as a Compensatory
396   Mechanism to the Impacts of Ocean Acidification. *Environmental Science & Technology*,
397   **51**, 2652–2659.

398   Mann ME, Zhang Z, Hughes MK, Bradley RS, Miller SK, Rutherford S, Ni F (2008) Proxy-
399   based reconstructions of hemispheric and global surface temperature variations over the past
400   two millennia. *Proc. Natl. Acad. Sci.*, **105**, 13252–13257.
401   McCoy SJ, Pfister CA (2014) Historical comparisons reveal altered competitive interactions in a
402   guild of crustose coralline algae (ed Jackson S). *Ecology Letters*, **17**, 475–483.
403   McCoy SJ, Ragazzola F (2014) Skeletal trade-offs in coralline algae in response to ocean
404   acidification. *Nature Climate Change*, **4**, 719–723.
405   McMillan AD (2000) *Since the time of the transformers: the ancient heritage of the Nuu-Chah-*
406   *Nulth, Ditidaht, and Makah.*
407   Melzner F, Stange P, Trübenbach K et al. (2011) Food Supply and Seawater pCO2 Impact
408   Calcification and Internal Shell Dissolution in the Blue Mussel Mytilus edulis. *PLoS ONE*, **6**,
409   e24223.
410   Mount AS, Wheeler AP, Paradkar RP, Snider D (2004) Hemocyte-mediated shell mineralization
411   in the eastern oyster. *Science*, **304**, 297–300.
412   Nash MC, Opdyke BN, Troitzsch U et al. (2012) Dolomite-rich coralline algae in reefs resist
413   dissolution in acidified conditions. *Nature Climate Change*, **2**, 1–5.
414   Orr JC, Fabry VJ, Aumont O et al. (2005) Anthropogenic ocean acidification over the twenty-
415   first century and its impact on calcifying organisms. *Nature*, **437**, 681–686.
416   Ovaskainen O, Skorokhodova S (2013) Community-level phenological response to climate
417   change. *Proc. Natl. Acad. Sci.*, **110**, 13434-13439.
418   O'Donnell MJ, George MN, Carrington E (2013) Mussel byssus attachment weakened by
419   ocean acidification. *Nature Climate Change*, **18**, 135–5.
420   Palmer AR (1983) Relative cost of producing skeletal organic matrix versus calcification:
421   Evidence from marine gastropods. *Marine Biology*, **75**, 287–292.
422   Pauly M, Kamenos NA, Donohue P, LeDrew E (2015) Coralline algal Mg-O bond strength as a
423   marine pCO2 proxy. *Geology*, **43**, 267–270.
424   Pérez-Huerta A, Cusack M, McDonald S, Marone F, Stampanoni M, MacKay S (2009)
425   Brachiopod punctae: A complexity in shell biomineralisation. *Journal of Structural Biology*,
426   **167**, 62–67.
427   Pfister CA, McCoy SJ, Wootton JT, Martin PA, Colman AS, Archer D (2011) Rapid
428   Environmental Change over the Past Decade Revealed by Isotopic Analysis of the California
429   Mussel in the Northeast Pacific. *PLoSone*, **6**, e25766.
430   Pfister CA, Roy K, Wootton JT, McCoy SJ, Paine RT, Suchanek TH, Sanford E (2016)
431   Historical baselines and the future of shell calcification for a foundation species in a
432   changing ocean. *Proceedings of the Royal Society B: Biological Sciences*, **283**, 20160392–8.
433   Ries JB (2005) Aragonite production in calcite seas: effect of seawater Mg/Ca ratio on the
434   calcification and growth of the calcareous alga *Penicillus capitatus*. *Paleobiology*, **31**, 445–
435   458.
436   Ries JB, Anderson MA, Hill RT (2008) Seawater Mg/Ca controls polymorph mineralogy of
437   microbial $CaCO_3$: A potential proxy for calcite-aragonite seas in Precambrian time.
438   *Geobiology*, **6**, 106–119.
439   Stearns SC (1989) The evolutionary significance of phenotypic plasticity. *BioScience*, **39**, 436–
440   445.
441   Stumpp M, Wren J, Melzner F, Thorndyke MC, Dupont ST (2011) CO2 induced seawater
442   acidification impacts sea urchin larval development I: Elevated metabolic rates decrease
443   scope for growth and induce developmental delay. *Comparative Biochemistry and*

444   *Physiology, Part A*, **160**, 331−340.
445 Suchanek TH (1992) Extreme biodiversity in the marine environment - Mussel bed communities
446   of *Mytilus californianus*. *Northwest Environmental Journal*, **8**, 150−152.
447 Thomsen J, Melzner F (2010) Moderate seawater acidification does not elicit long-term
448   metabolic depression in the blue mussel Mytilus edulis. *Marine Biology*, **157**, 2667−2676.
449 Thomsen J, Gutowska MA, Saphörster J et al. (2010) Calcifying invertebrates succeed in a
450   naturally CO_2-rich coastal habitat but are threatened by high levels of future acidification.
451   *Biogeosciences*, **7**, 3879−3891.
452 Thomsen J, Haynert K, Wegner KM, Melzner F (2015) Impact of seawater carbonate chemistry
453   on the calcification of marine bivalves. *Biogeosciences*, **12**, 4209−4220.
454 Vermeij GJ (1976) Interoceanic differences in vulnerability of shelled prey to crab predation.
455   *Nature*, **260**, 135−136.
456 Wahl M, Buchholz B, Winde V et al. (2015) A mesocosm concept for the simulation of near-
457   natural shallow underwater climates: The Kiel Outdoor Benthocosms (KOB). *Limnology and*
458   *Oceanography: Methods*, **13**, 651−663.
459 Waldbusser GG, Brunner EL, Haley BA, Hales B, Langdon CJ, Prahl FG (2013) A
460   developmental and energetic basis linking larval oyster shell formation to acidification
461   sensitivity. *Geophysical Research Letters*, **40**, 2171−2176.
462 Weiner S, Addadi L (2011) Crystallization Pathways in Biomineralization. *Annual Review of*
463   *Materials Research*, **41**, 21−40.
464 Weiss IM, Tuross N, Addadi L, Weiner S (2002) Mollusc larval shell formation: amorphous
465   calcium carbonate is a precursor phase for aragonite. *Journal of Experimental Zoology*, **293**,
466   478−491.
467 Wootton JT, Pfister CA (2012) Carbon System Measurements and Potential Climatic Drivers at a
468   Site of Rapidly Declining Ocean pH (ed Chin W-C). *PLoS ONE*, **7**, e53396.
469 Wootton JT, Pfister CA, Forester JD (2008) Dynamic patterns and ecological impacts of
470   declining ocean pH in a high-resolution multi-year dataset. *Proc. Natl. Acad. Sci.*, **105**,
471   18848−18853.
472
473

474 **Figure legends**

475 Figure 1. EBSD analysis of midden mussel shells from 1060-1170 AD showing calcite

476 crystallographic orientation map in reference to the {0001} plane, according to color key. EBSD

477 scans centered on a summer growth band from the center of the shell record (middle-age of

478 individual), with most recent shell material at the bottom. Winter bands identified by horizontal

479 bands of condensed crystal sizes and higher relative concentration of organic matter, revealed by

480 black areas in the absence of crystal backscatter. A) Shell TI09001, aged 1170 yBP, scale bar 60

481 μm; B) Shell TI09004, aged 1100 yBP, scale bar 60 μm; C) Shell TI09007, aged 1060 yBP,

482 scale bar 60 μm. Refer to Fig. S2 for an illustration of crystal orientation. Fig. S3 shows a full

483 transect of shell TI09001. Fig. S4 shows additional scans of shell TI09007. These scans reveal

484 similar crystallographic orientation as that visible in shells from the 1970s and 2000s (Fig. 2,3),

485 with some evidence of shell fragility likely caused by ~1,000 years spent in middens.

486

487 Figure 2. EBSD analysis of archival shells collected 1975 (visible growth band ~1970) showing

488 calcite crystallographic orientation map in reference to the {0001} plane, according to color key.

489 EBSD scans centered on a summer growth band from the center of the shell record (middle-age

490 of individual), with most recent shell material at the bottom. Winter bands identified by

491 horizontal bands of condensed crystal sizes and higher relative concentration of organic matter,

492 revealed by black areas in the absence of crystal backscatter. A) Shell TS10002, scale bar 60 μm;

493 B) Shell TS10004, scale bar 60 μm. Refer to Fig. S2 for an illustration of crystal orientation.

494 These scans and those from modern 2000s shells (Fig. 3) provide reference for typical shell

495 crystallographic orientation in biogenic calcite.

496

497   Figure 3. EBSD analysis of modern 2000s shells collected 2009 (visible growth band ~2004)

498   showing calcite crystallographic orientation map in reference to the {0001} plane, according to

499   color key. EBSD scans centered on a summer growth band from the center of the shell record

500   (middle-age of individual), with most recent shell material at the bottom. Winter bands identified

501   by horizontal bands of condensed crystal sizes and higher relative concentration of organic

502   matter, revealed by black areas in the absence of crystal backscatter. A) Shell GL09002, scale

503   bar 60 μm; B) Shell HC09006, scale bar 60 μm. Refer to Fig. S2 for an illustration of crystal

504   orientation. Fig. S5 shows a full transect of Shell HC09006. These scans and those from archival

505   1970s shells (Fig. 2) provide reference for typical shell crystallographic orientation in biogenic

506   calcite.

507

508   Figure 4. EBSD analysis of modern 2010s shells collected 2015 (visible growth band ~2012)

509   showing calcite crystallographic orientation map in reference to the {0001} plane, according to

510   color key. EBSD scans centered on a summer growth band from the center of the shell record

511   (middle-age of individual), with most recent shell material at the bottom. Winter bands identified

512   by horizontal bands of condensed crystal sizes and higher relative concentration of organic

513   matter, revealed by black areas in the absence of crystal backscatter. A) Shell GL15007, scale

514   bar 60 μm; B) Shell GL15005, scale bar 60 μm; C) Shell HC15003, scale bar 60 μm; and D)

515   Shell HC15004, scale bar 70 μm. Refer to Fig. S6 for additional images and to Fig. S2 for an

516   illustration of crystal orientation. These shells show distinct areas of amorphous calcium

517   carbonate, particularly in panels B and C, and suggest variability between individuals.

518

519   Figure 5. A) Raman peak full width at half peak maximum (FWHM), indicating Mg-O bond

520   strength, and Raman shift (cm^{-1}), indicating Mg content. B) Standard deviations plotted by site

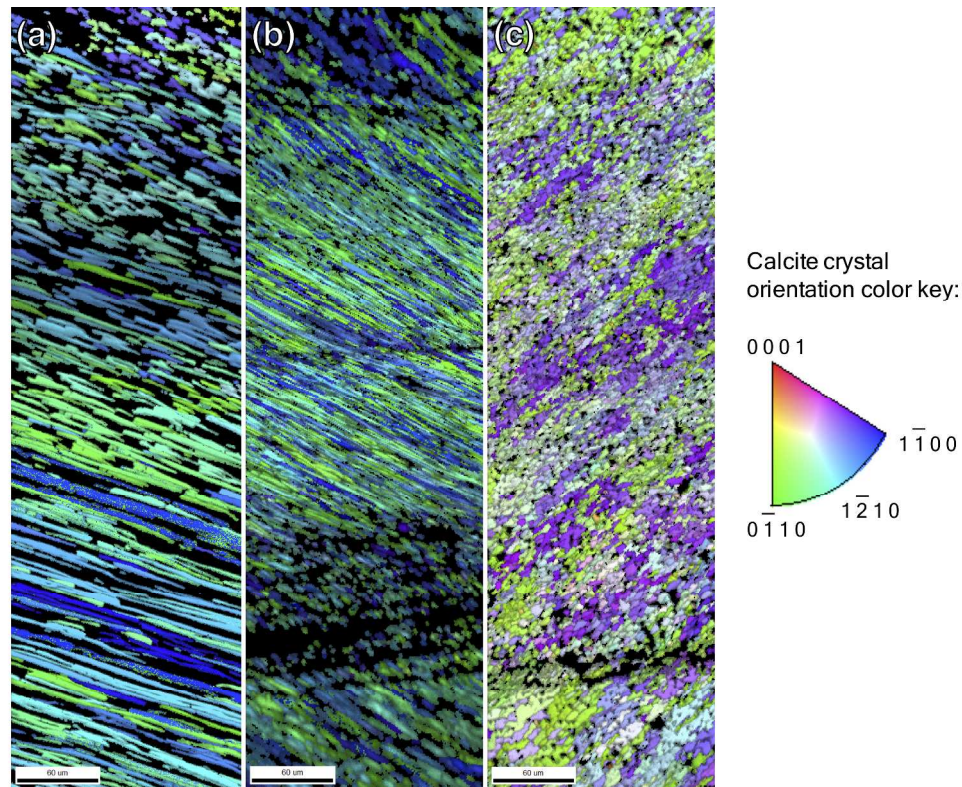521   and era. Overlapping points appear more vivid.

Figure 1. EBSD analysis of midden mussel shells from 1060-1170 AD showing calcite crystallographic orientation map in reference to the {0001} plane, according to color key. EBSD scans centered on a summer growth band from the center of the shell record (middle-age of individual), with most recent shell material at the bottom. Winter bands identified by horizontal bands of condensed crystal sizes and higher relative concentration of organic matter, revealed by black areas in the absence of crystal backscatter. A) Shell TI09001, aged 1170 yBP, scale bar 60 m; B) Shell TI09004, aged 1100 yBP, scale bar 60 m; C) Shell TI09007, aged 1060 yBP, scale bar 60 m. Refer to Fig. S2 for an illustration of crystal orientation. Fig. S3 shows a full transect of shell TI09001. Fig. S4 shows additional scans of shell TI09007. These scans reveal similar crystallographic orientation as that visible in shells from the 1970s and 2000s (Fig. 2,3), with some evidence of shell fragility likely caused by ~1,000 years spent in middens.
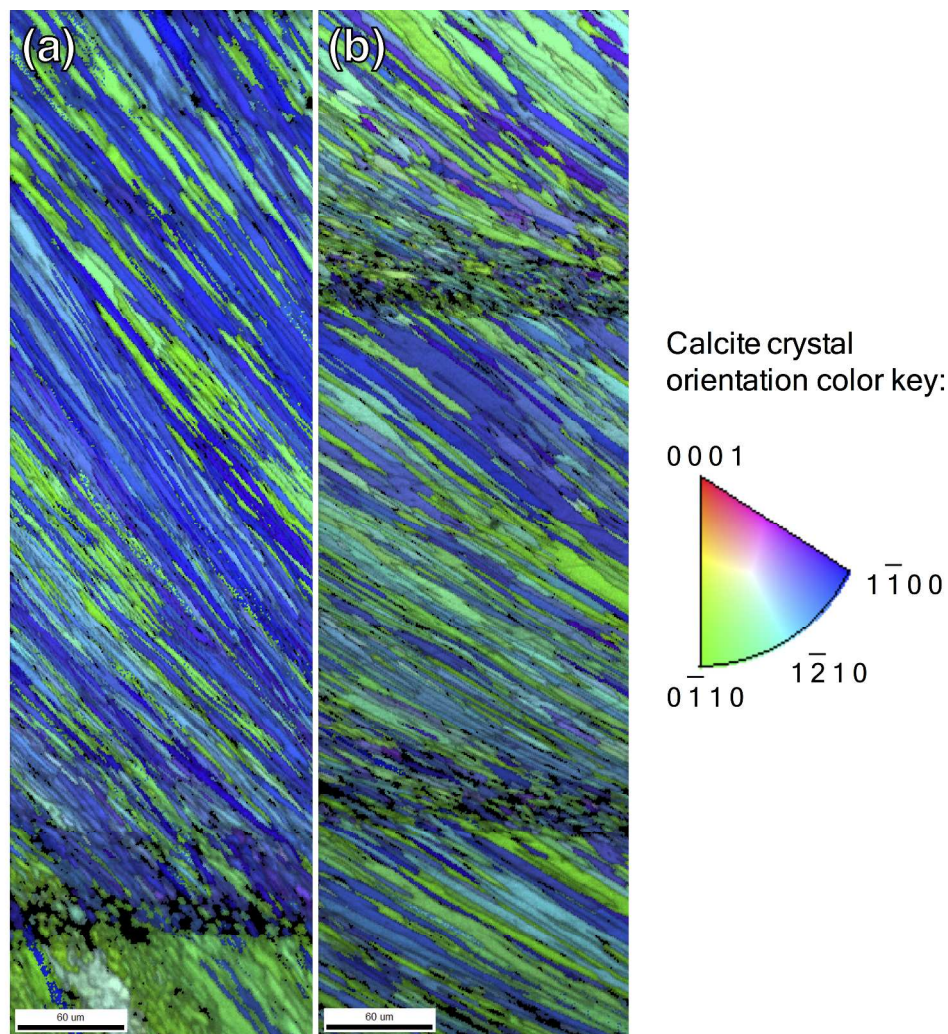
Figure 2. EBSD analysis of archival shells collected 1975 (visible growth band ~1970) showing calcite crystallographic orientation map in reference to the {0001} plane, according to color key. EBSD scans centered on a summer growth band from the center of the shell record (middle-age of individual), with most recent shell material at the bottom. Winter bands identified by horizontal bands of condensed crystal sizes and higher relative concentration of organic matter, revealed by black areas in the absence of crystal backscatter. A) Shell TS10002, scale bar 60 m; B) Shell TS10004, scale bar 60 m. Refer to Fig. S2 for an illustration of crystal orientation. These scans and those from modern 2000s shells (Fig. 3) provide reference for typical shell crystallographic orientation in biogenic calcite.
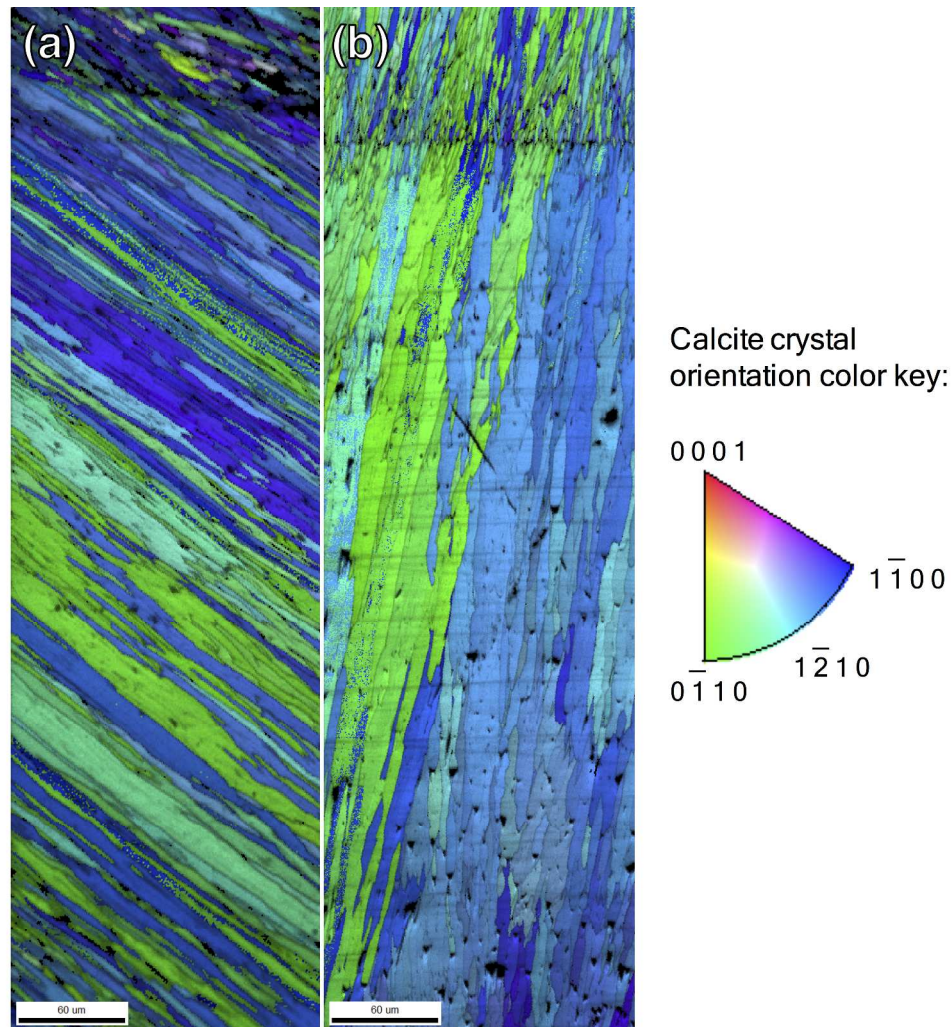
Figure 3. EBSD analysis of modern 2000s shells collected 2009 (visible growth band ~2004) showing calcite crystallographic orientation map in reference to the {0001} plane, according to color key. EBSD scans centered on a summer growth band from the center of the shell record (middle-age of individual), with most recent shell material at the bottom. Winter bands identified by horizontal bands of condensed crystal sizes and higher relative concentration of organic matter, revealed by black areas in the absence of crystal backscatter. A) Shell GL09002, scale bar 60 m; B) Shell HC09006, scale bar 60 m. Refer to Fig. S2 for an illustration of crystal orientation. Fig. S5 shows a full transect of Shell HC09006. These scans and those from archival 1970s shells (Fig. 2) provide reference for typical shell crystallographic orientation in biogenic calcite.
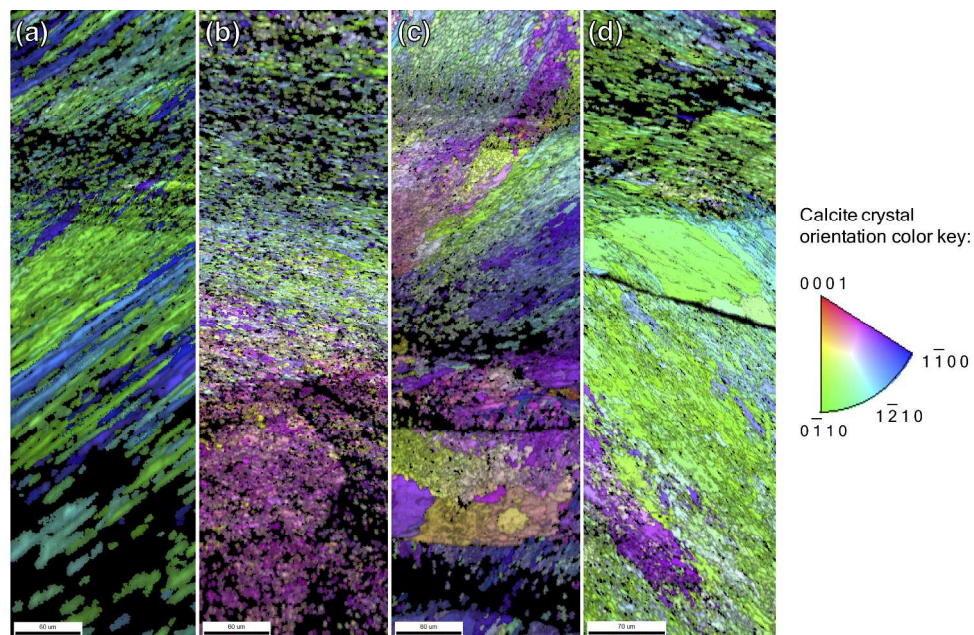
Figure 4. EBSD analysis of modern 2010s shells collected 2015 (visible growth band ~2012) showing calcite crystallographic orientation map in reference to the {0001} plane, according to color key. EBSD scans centered on a summer growth band from the center of the shell record (middle-age of individual), with most recent shell material at the bottom. Winter bands identified by horizontal bands of condensed crystal sizes and higher relative concentration of organic matter, revealed by black areas in the absence of crystal backscatter. A) Shell GL15007, scale bar 60 m; B) Shell GL15005, scale bar 60 m; C) Shell HC15003, scale bar 60 m; and D) Shell HC15004, scale bar 70 m. Refer to Fig. S6 for additional images and to Fig. S2 for an illustration of crystal orientation. These shells show distinct areas of amorphous calcium carbonate, particularly in panels B and C, and suggest variability between individuals.
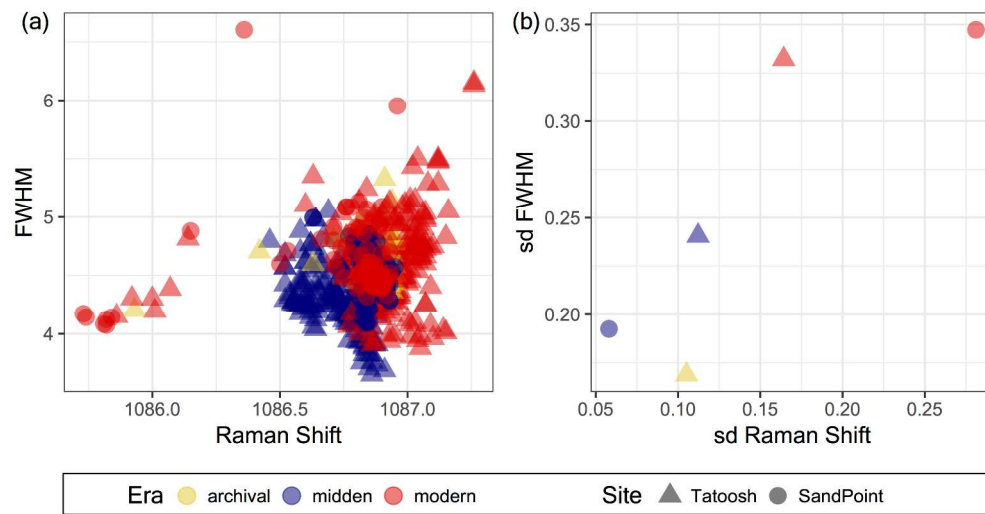
Figure 5. A) Raman peak full width at half peak maximum (FWHM), indicating Mg-O bond strength, and Raman shift (cm-1), indicating Mg content. B) Standard deviations plotted by site and era. Overlapping points appear more vivid.